Tailoring of functionally graded hyperelastic materials via grayscale mask stereolithography 3D printing

Iman Valizadeh[a,*], Ahmad Al Aboud[b], Edgar Dörsam[b], Oliver Weeger[a]

[a] *Cyber-Physical Simulation Group, Department of Mechanical Engineering & Center for Computational Engineering, Technical University of Darmstadt, Dolivostr. 15, Darmstadt, 64293, Hessen, Germany*
[b] *Institute of Printing Science and Technology, Technical University of Darmstadt, Magdalenenstr. 2, Darmstadt, 64289, Hessen, Germany*

Abstract

Photopolymerization-based additive manufacturing methods like stereolithography and digital light processing only allow typically the monolithic fabrication of structures made from a single material. To overcome this limitation, grayscale digital light processing has been proposed for 3D printing of functionally graded materials. Here, this concept is extended to grayscale masked stereolithography (MSLA) printing using a LED light source and a LCD photomask to control the degree of photopolymerization of a UV-curable resin by varying grayscale pixels and thus light intensities. In this scale, tailorable hyperelastic material properties and functionally graded structures for finite deformations are realized. In this paper, the dependency of the resulting material properties on the parameters of the grayscale MSLA process is investigated and a grayscale-dependent hyperelastic material model is formulated. This parametric hyperelastic material model is fitted to the experiments and validated against experimental results for uniaxial tension and uniaxial compression tests. Then, functionally graded structures with tailored mechanical properties at finite deformations are designed and fabricated using grayscale MSLA printing. The hyperelastic material model is validated with experimental results for different geometries, showing good agreement between experimental tests and numerical calculations.

Keywords: Additive manufacturing, stereolithography, hyperelastic materials, functionally graded materials

1. Introduction

Additive manufacturing or specifically 3D printing of polymeric materials is a growing favorable manufacturing technology, which enables fabrication of intricate 3D structures with high resolution and rapid speed [1, 2, 3, 4, 5]. It has great potentials and application fields in bioengineering [6, 7, 8, 9, 10], food production [11], high-performance materials [12, 13], robotics [14, 15], 4D printing and functional materials [16, 17, 18, 19, 20] and electronic devices [21, 22, 23].

In general, for fabrication of plastics and polymeric materials, three types of additive manufacturing concepts can be distinguished: extrusion and fusion of solid filaments (FFF, FDM), laser sintering of solid powders (SLS), and photocuring of liquid resins (SLA, DLP, inkjet) [24]. While each of these techniques has their own advantages and challenges, we focus here on vat photopolymerization based methods, which are often coined as stereolithography. Briefly, in all vat photopolymerization processes, a reservoir of UV-curable, liquid resin is exposed to UV light in order to form chains between the molecules and chemically crosslink them. In this way, a solid 3D geometry is created through layer-by-layer photocuring of the resin. This type of process is applicable to a wide range of materials, including biomaterials, ceramics, glass, shape-memory polymers, and electronics [25]. Furthermore, it offers high accuracy with printing resolutions ranging from micro- to nanometer scales. While laser-based stereolithog-

*corresponding author
Email address: iman.valizadeh@tu-darmstadt.de (Iman Valizadeh)

Accepted manuscript, *Additive Manufacturing*, DOI 10.1016/j.addma.2021.102108

raphy (SLA) is generally slow, since a single leaser beam is moved around the printing area, digital light processing (DLP) and masked stereolithography (MSLA) are much faster, since they use a light projector and LED arrays with LCD photomasks, respectively, and are thus more suitable for large-scale application [26].

However, a general disadvantage of vat photopolymerization methods compared to FFF and material jetting is that only a single material can be printed at once. This limits the applicability for fabrication of multi-material objects with heterogeneous, functionally graded material properties [27, 28, 29, 30], which have already been demonstrated successfully in particular for inkjet 3D printing of photopolymers [31, 32, 33], however, limited to small strains and stresses. While systems with multiple vats and materials are difficult to realize [34, 35], MSLA can overcome this limitation by modulating the degree of curing of the photopolymer, which can be controlled in terms of the light intensity through grayscale masks [36, 37, 19, 38]. Thus, functionally graded objects can not only be realized by vat photopolymerization with user-defined digital masks that generate microstructures [38, 39, 40, 41], but also by underexposing the material through grayscale pixels, which produce in general weaker mechanical properties and lower stiffness as a result of the lower cross-linking density [19, 42, 17, 44]. Therefore, the mechanical properties of pixels, or rather material points, can be controlled by changing light intensity through grayscale masks. This yields the possibility of making graded structures with tunable mechanical material properties, as well as meta- and high-performance materials [45, 17, 20].

Although previous investigations have revealed that grayscale values and variation of printing time enable tunable mechanical properties of printed materials [42, 43, 19], there have been few attempts at constitutive modeling of printed materials as a function of grayscale values and process parameters at finite deformations. A recent investigation shows the influence of the light intensity on a photocured polymer by describing a visco-hyperelastic model [46]. Similarly, (visco-) hyperelastic constitutive models have already been formulated for a FFF-printed thermoplastic elastomer (TPE) in [47] and for inkjet printed photopolymers in [48, 49]. Furthermore, in the research of [50], experiments were carried out to derive a relationship between visco-hyperelatic material properties and crosslinking density of photopolymerized materials. In general, elastomers are typically modeled at finite deformations with constitutive equations of (visco-) hyperelasticity, in which an energy function represents the material response to deformation, which is often expressed in terms of invariants of the deformation measures [51]. Particularly, a widely used material model for describing elastomers and rubber-like materials is the three parameter polynomial hyperelastic material model, called generalized Rivlin model, which is formulated in terms of the invariants of the right Cauchy-Green tensor [52, 53, 51]. In recent studies, this model exhibited better accuracy than other hyperelastic constitutive models in modeling of hydrogels [54]. Furthermore, it has also been successfully used for modeling of 3D printed soft metamaterials [55] and extended to the modeling of 4D printed shape memory polymers [56].

This research presents a hyperelastic, finite deformation constitutive model for a MSLA printed material, for which the parameters depend on the grayscale values of the mask. For this purpose, specimens for standard uniaxial tension, uniaxial compression and volumetric compression tests are fabricated with a commercial MSLA 3D printer, here the Original Prusa SL1 [57], at different grayscale values. By fitting a Mooney-Rivlin constitutive model to the test data, it is seen that the material constants vary with grayscale values. Therefore, the material constants are parameterized as a function of the grayscale value. The proposed grayscale hyperelastic formulation is validated by printing further specimens at arbitrary grayscale values and comparing the finite deformation material response of experimental tests with numerical solutions obtained using the parametric model. The developed hyperelastic formulation can be used in engineering problems and computational simulations with arbitrary loading conditions. Thus, it facilitates the design of functionally graded structures with spatially varying material behavior that can be easily and precisely controlled by the grayscale value.

The further outline of this manuscript is as follows: Section 2.1 describes the grayscale masked stereolithography and its influence on polymerization of photosensitive polymers. In addition, the slicing process and the structure of projection-based printers are discussed in this section. The fundamental of hyperelastic material modeling and the material model is pointed out in Section 2.2. The

technical aspects and methodology of this work are given in Section 2.3. Finally, the results are demonstrated and discussed in Section 3, which contains characterizing and validation of the material model in 3.1 and 3.2, and the application of the graded structure in 3.3.

2. Methods

2.1. Tailoring material properties by grayscale masked stereolithography

In this section, we want to briefly discuss the basic working principles of masked stereolithography 3D printing and how it can be used to tailor and grade the resulting material properties through grayscale masks.

A masked stereolithography 3D printer consists of a UV light source, a LCD module, zoom and projection lenses, the resin tank with transparent bottom, and the printing platform , which is shown schematically in Fig. 1. Within MSLA printing, the UV light is transmitted from the light source onto the LCD chip, which reflects the filtered light to the optic lenses. The optic lenses regulate the transmitted area and focus the incident light on the tank holding the liquid photopolymer resin. At the bottom interface of the transparent tank, where the light penetrates in the liquid resin, photopolymerization takes place and solidifies the resin. To capture the solidified material, a print platform is dipped into the tank such that the first layer of polymer attaches to the platform. By repeatedly lifting the platform and switching on the light source, 3D structures are then built up layer-by-layer.

In this process, the light attenuation is an important parameter, which affects the printing time, resolution and quality of the printed objects [58, 38], as well as the resulting material parameters. The light power is reduced from the light source to the platform due to the reflection, propagation and filtering of light through the chip, LCD and optic lenses [58, 59]. In particular, the incident UV light is filtered by the LCD to irradiate only selected pixels on the tank interface. Once the digital mask is uploaded in the LCD, the alignment of liquid crystals changes concerning the color of the pixels of the mask, which could be white or black, meaning that the respective pixel is either fully irradiated or not cured at all. At the interface of the tank, the transmitted light causes the excitation of free radicals by

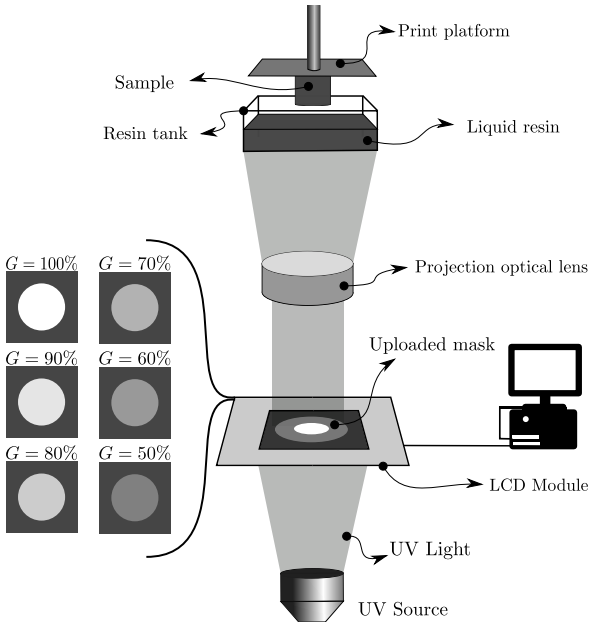

Figure 1: Schematic illustration of a projection-based printer (MSLA), which typically consists of a UV light source, LCD module containing liquid crystals, zoom and projection lenses, and printer platform. The grayscale $G = 100\%$ represents full light intensity being transmitted by the LCD mask with RGB $= (255, 255, 255)$, while $G = 0\%$ represents no light transmissions with RGB $= (0, 0, 0)$.

a photoinitiator. Then, long-chain molecules are formed under the initiation of those free radicals due to the reaction of prepolymers with each other. By initiation and propagation of radicals into larger areas, the process of building long-chain molecules continues, enhancing the cross-link density and finally forming a solid state by joining the long-chain molecules together [58]. Almost full cross-linking is performed for the white pixels subjected to the complete light intensity. For more details on photopolymerization and cross-linking during printing see [60, 63] among others.

The degree of curing of the photopolymer, i.e., its cross-linking density, increases with intensity and duration of the irradiation, such that the polymer can be considered as fully cured when subject to a sufficient amount of luminous energy [58, 38, 64]. Thus, it is influenced by the power of the UV light source and the light attenuation from source to tank, which are fixed for a given printer setup. Furthermore, it can be controlled by the printing time per layer and the layer thickness, which may be

changed from layer to layer, but not within a layer. The mask, however, can not only be used to set either full or zero light intensity for different material points within the same layer through white or black pixels, respectively, but also to regulate light intensity through grayscale values. As the light intensity varies, the cross-linking density varies, which influences the material properties in a locally adjustable manner [19, 20].

To realize structures with graded material properties through variation of cross-linking density, grayscale masks must be uploaded to the LCD for each layer. Typically, a slicer software is used to create such masks from a 3D geometry as a stack of black-and-white images. In these 8-bit bitmaps, white pixels with RGB $= (255, 255, 255)$ represent full light intensity, while black pixels with RGB $= (0, 0, 0)$ yield no exposure at all, i.e., leave the photopolymer at the material point uncured. Now, grayscale values can be simply defined as intermediate RGB values. In the context of grayscale MSLA and SLA-DLP printing methods, there are various definitions for "grayscale values" in the literature. Some references define grayscale values as the percentage of the maximum light intensity, by measuring light intensity, while others consider it as the percentage of RGB value or even the RGB value itself [19, 42, 20]. In this work, the grayscale value G refers to a percentage of the RGB value, i.e. $G = 100\%$ refers to RGB $= (255, 255, 255)$, $G = 50\%$ to RGB $= (128, 128, 128)$, and $G = 0\%$ to RGB $= (0, 0, 0)$. However, it should be noted that the light intensity varies nonlinearly with RGB value and so does G [15, 20]. Fig. 1 also illustrates the grayscale representation. Although any arbitrary grayscale can be applied to the masks, we limit G to 50% to 100% in this work, since for lower values the cross-linking density is insufficient, i.e., the specimens can not be printed or have considerable deformities and geometrical errors [42].

2.2. Hyperelastic constitutive modeling for grayscale printed materials

In this section, the hyperelastic material modeling methodology for grayscale printed polymers is explained briefly.

The printed photopolymers are fundamentally classified as rubber-like elastomers, which exhibit a nonlinear stress-strain relation, are almost incompressible under external forces, can undergo finite elastic deformations, and have small volumetric changes under compression [53]. Furthermore, they can be assumed to exhibit direction-independent, i.e., isotropic, material behavior [61, 62]. At finite deformations, these types of incompressible or nearly-incompressible materials are typically modeled with hyperelastic constitutive models, which are based on energy function and can be formulated in terms of invariants of the deformation measures [51]. A well-established hyperelastic constitutive model for describing elastomers and rubber-like materials is the three parameters polynomial model, called generalized Rivlin model, which is based on the invariants of the right Cauchy-Green tensor [52, 53, 51].

Within the theory of finite hyperelasticity, the existence of a strain energy density function $\psi(\mathbf{F})$ is assumed, where $\mathbf{F}$ is the deformation gradient [65]. This Helmholtz free-energy function can also be expressed in terms of the symmetric right Cauchy-Green strain tensor $\mathbf{C} = \mathbf{F}^\top \mathbf{F}$, and in the isotropic case only its invariants, as

$$\psi(\mathbf{C}) = \psi(I_1, I_2, I_3)\,, \tag{1}$$

in which $I_a, a = 1, 2, 3$ are the invariants of $\mathbf{C}$ as

$$\begin{aligned} I_1 &= \mathrm{tr}(\mathbf{C}) = \lambda_1^2 + \lambda_2^2 + \lambda_3^2, \\ I_2 &= \frac{1}{2}\left[(\mathrm{tr}(\mathbf{C}))^2 - \mathrm{tr}(\mathbf{C}^2)\right] \\ &= \lambda_1^2\lambda_2^2 + \lambda_1^2\lambda_3^2 + \lambda_2^2\lambda_3^2, \\ I_3 &= \det(\mathbf{C}) = \lambda_1^2\lambda_2^2\lambda_3^2\,, \end{aligned} \tag{2}$$

with principal stretches $\lambda_i, i = 1, 2, 3$. The incompressibility condition for elastomers is denoted as $J = \det(\mathbf{F}) = \lambda_1\lambda_2\lambda_3 = 1$, with J representing the volume ratio of an infinitesimal volume element in spatial and material configurations, $J = dv/dV$. This formulation of the strain energy density function in terms of invariants guarantees its symmetry and objectivity [66].

Since some materials exhibit different behavior in bulk and shear, and the incompressibility constraint arises straight from volumetric strain, it can be more beneficial to express strain energy function with two distinct parts in terms of dilational (volume-changing) and distortional (volume-preserving, isochoric) contributions [65, 53]. Therefore, equation (1) can be written for a nearly incompressible material as

$$\psi = \psi(I_1, I_2, J) = \psi_{\mathrm{vol}}(J) + \psi_{\mathrm{iso}}(I_1, I_2)\,, \tag{3}$$

where ψ_{vol} and ψ_{iso} are the dilational and distor-

tional terms, respectively. Due to the second law of thermodynamics and the Coleman–Noll procedure, the first Piola–Kirchhoff stress for a hyperelastic material is obtained from the strain energy function as

$$\begin{aligned}\mathbf{P} &= \frac{\partial \psi(I_1, I_2, I_3)}{\partial \mathbf{F}} = 2 \sum_{i=1}^{3} \frac{\partial \psi}{\partial I_i} \frac{\partial I_i}{\partial \mathbf{F}} \\ &= \mathbf{P}_{\text{vol}} + \mathbf{P}_{\text{iso}} \\ \text{with} \quad \mathbf{P}_{\text{vol}} &= \frac{\partial \psi_{\text{vol}}}{\partial \mathbf{F}} \quad \text{and} \quad \mathbf{P}_{\text{iso}} = \frac{\partial \psi_{\text{iso}}}{\partial \mathbf{F}} \,.\end{aligned} \tag{4}$$

Further details on stress tensors and their derivations can be found for instance in [65].

The concrete formulation of the energy function in terms of $\mathbf{F}, \mathbf{C}$, or the invariants, determines the material behavior under loading within the constitutive theory of finite elasticity. Accordingly, the choice of material model depends on its application and inherent behavior under experimental tests. Here, the Mooney-Rivlin model is chosen to express the hyperelastic constitutive behavior of grayscale 3D printed polymer materials, since it is well-established for modeling of elastomers undergoing large strains. For fitting the experimental characterization data of the material at hand here, this model is most suitable, however, for other materials other models might certainly be investigated and turn out to be more appropriate. The general formulation of the Mooney-Rivlin hyperelastic material model for an incompressible material is given[52, 53] as

$$\begin{aligned}\psi &= \psi(I_1, I_2, J) \\ &= \frac{1}{d}(J-1)^2 + \sum_{m=0}^{M} \sum_{n=0}^{N} C_{mn} \, (I_1 - 3)^m \, (I_2 - 3)^n \,,\end{aligned} \tag{5}$$

where d is the incompressibility constant and C_{mn} represent the further material constants, where $C_{00} = 0$, These material parameters have to be determined through curve fitting of experimental test data. In this research, we use the Mooney-Rivlin material model with three parameters, which results from equation (5) by setting $M = N = 1$ as

$$\begin{aligned}\psi(I_1, I_2, J) = \frac{1}{d}(J-1)^2 + C_{10}(I_1 - 3) \\ + C_{01}(I_2 - 3) + C_{11}(I_1 - 3)(I_2 - 3) \,.\end{aligned} \tag{6}$$

The stress state is calculated from (4) for a given strain state as

$$\begin{aligned}\mathbf{P}(\mathbf{F}) =& \frac{2}{d}(J-1)\,\text{cof}(\mathbf{F}) + 2\frac{\partial \psi}{\partial I_1}\mathbf{F} \\ &+ 2\frac{\partial \psi}{\partial I_2}\left(I_1 \mathbf{F} - \mathbf{F}\mathbf{C}\right) \\ =& \frac{2}{d}(J-1)\,\text{cof}(\mathbf{F}) + 2\left(C_{10} + C_{11}(I_2 - 3)\right)\mathbf{F} \\ &+ 2\left(C_{01} + C_{11}(I_1 - 3)\right)\left(I_1 \mathbf{F} - \mathbf{F}\mathbf{C}\right) \,.\end{aligned} \tag{7}$$

The unknown parameters in the equation (6) can be determined like the stress state $\mathbf{P}(\mathbf{F})$ which calculated from the model agrees with the stress state resulting from experiments for various loading conditions and known strain states $\mathbf{F}$. To completely determine the material parameters, several experiments with different loading conditions are required [66, 67]. Therefore, a volumetric compression test is carried out to determine the incompressibility constant d, and uniaxial tension and compression tests are carried out to investigate the response of the material in Cartesian directions toward finding the material constants C_{mn}.

Furthermore, the objective here is to formulate a material model that is parameterized in terms of the grayscale value G as

$$\begin{aligned}\psi(G) &= \psi(I_1, I_2, J; G) \\ &= \frac{2}{d(G)}(J-1)^2 + C_{10}(G)\,(I_1 - 3) \\ &+ C_{01}(G)\,(I_2 - 3) + C_{11}(G)\,(I_1 - 3)(I_2 - 3).\end{aligned} \tag{8}$$

Here, the four material constants $d, C_{10}, C_{01}, C_{11}$ are functions of G, which will be achieved by interpolating the material constants fitted for different discrete values of G, see Section 2.3.

Furthermore, these Mooney-Rivlin coefficients can be converted to physical parameters of the material, namely the bulk modulus $\kappa = 2/d$ and the shear modulus $\mu = 2(C_{01} + C_{10})$. When restricting to linear elastic behavior, i.e., infinitesimal strains, the Young's modulus and Poisson's ratio can be determined by the Lamé parameter conversion formulas as $E = 9\kappa\mu/(3\kappa + \mu)$ and $\nu = (3\kappa - 2\mu)/(6\kappa + 2\mu)$, respectively. Besides the Mooney-Rivlin coefficients, also the grayscale-dependency of these physical parameters will be investigated.

Light source	UV LED
Wavelength	405 nm
Light intensity	ca. 990 mW/m^2
Mask	LCD
LCD display size	120 × 68 mm
Print volume	120 × 68 × 150 mm
XY-Resolution	0.047 mm
Layer thickness	0.050 mm
Initial exposure time	35 s
Initial exposure layers	10
Exposure time	10 s

Table 1: Technical data of MSLA 3D printer [57] and the print parameters used.

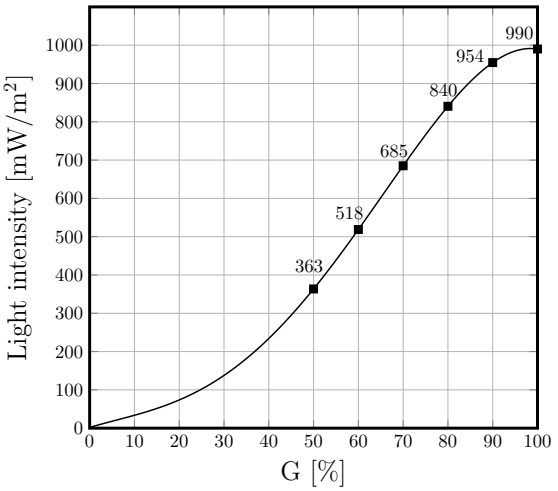

Figure 2: Dependence of the light intensity on the grayscale value G.

2.3. Experimental methodology and materials

The objective of this manuscript is formulate and fit a parametric material model based on grayscale values. For this aim, specimens are printed at different grayscale values G, i.e., with different levels of curing, and subsequently tested under various loading conditions, namely uniaxial tension, uniaxial compression, and volumetric compression.

For the manufacturing of specimens, the commercial MSLA-printer "Original Prusa SL1" is used. The properties of the printer and the print parameters used here are given in Tab. 1. Furthermore, the commercial, UV-sensitive "Orange Tough Resin" by Prusa Research a.s. is used. The composition of the material is provided by the producer as epoxy resin $40\% - 50\%$, monomer $20\% - 40\%$, color pigment $2\% - 5\%$, and photoinitiators $3\% - 5\%$.

The test samples are designed by using a CAD software, from which they are exported in STL file format. These files are then imported into the "PrusaSlicer" software, which generates the masks (slices) at a desired layer thickness (as PNG images). It is also used to set the printing parameters, i.e., exposure time for initial layers, number of these initial layers, as well as default exposure time for subsequent layers. Here, all specimens are printed with layer thickness of 0.05 mm, initial exposure time of 35 s over 10 layers, and exposure time of 10 s for all remaining layers. The light intensity regulated either through grayscale values or exposure time could have an identical influence on the curing of photopolymers under exposure of UV light [38, 58]. However, changing the exposure time has influence on a whole layer, while changing the grayscale affects the material of each pixel separately. Thus, in order to control the degree of polymerization, the exposure time here is fixed and the grayscale values of the pixels are varied. Since all samples are printed in an upright position, we assume that all material points with a certain assigned grayscale value are subject to the same dose of light and exhibit the same degree of cure, also for samples with graded grayscale values.

As mentioned previously, the masks generated by the slicer software contain only black and white pixels, where the white pixels illustrate the shape of the geometry to be printed at the respective layer. Theoretically, the light illuminates through the white pixels at full intensity. Therefore, tailoring of material properties is carried out by changing the RGB grayscale values of the pixels, which reduces the light intensity during the printing process. Here, MATLAB [68] is utilized for image processing and adjusting the grayscale values of white pixels. Three mechanical tests are carried out toward characterizing the strain energy function for each grayscale value G, i.e., uniaxial tension, uniaxial compression, and volumetric compression. The uniaxial tensile test is performed according to ASTM D638 standard, with sample type IV and test speed 5 mm/min. The compression test method is defined in ISO 7743 standard. The test type A and method A are performed on a cylindrical specimen with diameter 29±0.5 mm and height 12.5±0.5 mm. The volumetric compression test is performed on a cylindrical test specimen with diameter 17.8±0.15 mm and height 25±0.25 mm based on type B and method B. A length gauge with 0.2 μm repetition

accuracy is used to measure the length changes of test specimens to calculate the strain in the uniaxial tensile tests. A Zwick Z050 testing machine with ± 2 μm position repetition and 27 nm travel resolution accuracy is used to execute the tests.

The test specimens for all three test types are printed in $G = 100\%, G = 90\%, G = 80\%, G = 70\%, G = 60\%$, and $G = 50\%$, as shown schematically in Fig. 1. Based on the full light intensity of the printer of $990\,\mathrm{mW/m^2}$ and the relation between grayscale or RGB value and light intensity established in [19], a conversion of these grayscale values to light intensities is provided in Fig. 2. Nevertheless, for the actual design grayscales are directly specified through their corresponding RGB values. Each test is carried out for five specimens of each G-value, which results in a total of ninety experiments being performed. Then, the experimental results from each type of test are averaged for specific G-values, and the averaged value is used for the curve fitting process. Based on the parameters obtained at specified G-values, namely $G = 100\%, G = 90\%, G = 80\%, G = 70\%, G = 60\%$, and $G = 50\%$, the Mooney-Rivlin coefficients and the physical material parameters are parameterized in terms of G using linear and quadratic least-squares approximations for $50\% \leq G \leq 100\%$.

3. Results and discussion

In this section the experimental and numerical results for hyperelastic constitutive modeling of grayscaled printed materials are demonstrated, compared and discussed. First, in the grayscaled printed material is characterized and the hyperelastic material constants are determined (Section 3.1). Then, a verification of the hyperelastic material model is carried out (Section 3.2). Finally, the application of the material model is demonstrated by different test cases with graded samples (Section 3.3).

3.1. Characterization of grayscale printed materials

To characterize the mechanical response of grayscale 3D printed materials with $G = 100\%, G = 90\%, G = 80\%, G = 70\%, G = 60\%$, and $G = 50\%$ under different deformation states, volumetric compression, uniaxial tension and uniaxial compression tests are carried out, and their resulting stress-strain curves are shown in Fig. 3a, Fig. 3b and Fig. 3c, respectively. As can be seen in particular in the uniaxial tension test in Fig. 3a, the materials behave fairly nonlinear with softening at higher strains. Furthermore, the stiffness generally increases with grayscale value, yielding higher stresses. In addition, the failure strains and stresses increase with grayscale. Volumetric compression responses shown in Fig. 3c are fairly similar, since the materials are nearly incompressible.

Now, the Mooney-Rivlin constants are determined such that the stresses obtained from the material model (7) fit the experimental averages of the stress-strain curves for each grayscale G. This curve fitting process is carried out through a least-squares optimization technique for (nearly) incompressible hyperelastic material models, as described in [67]. First, the incompressibility parameter d is obtained from the volumetric test, then the remaining coefficients C_{01}, C_{10}, C_{11} are fitted to the uniaxial compression and tension tests. The results of the curve fitting are demonstrated in Fig. 4, which shows a good agreement of the experimental average curves for uniaxial tension and compression with the Mooney-Rivlin models for all grayscales G. The obtained material coefficients d, C_{01}, C_{10} and C_{11} are illustrated in Fig. 5 and given in Tab. 2. Note that for each G, we obtained the same, unique values for the coefficients independently of the initial values specified for the optimization.

As can be seen in Fig. 5, the dependency of these coefficients on G appears to be rather nonlinear. d and C_{01} are both positive and monotonously increasing with G, while C_{10} is negative and decreases with G, i.e., its magnitude also increases with G. For C_{11}, which is also positive, the trend is less clear, but it generally also increases with G. Nevertheless, these coefficients can be reasonable well approximated in terms of G by a linear or quadratic fit of the experimentally obtained data points.

The behavior of the physical material parameters bulk modulus κ and shear modulus μ, as well as linear elastic parameters Young's modulus E and Poisson's ratio ν, which are calculated from the given relations at the end of Section 2.2, is shown in Fig. 6 and in Tab. 2 . Despite the dissimilar behavior of the coefficients $d, C_{01}, C_{10}, C_{11}$ of the Mooney-Rivlin material model, these Lamé parameters all exhibit a more monotonous behavior, in which the shear modulus, bulk modulus and Young's modulus increase almost linearly with grayscale from $G = 50\%$ to $G = 100\%$, and the Poisson's ratio decreases with G. These Lamé parameters can be parameterized in terms of G very well using linear and quadratic approximations, as can be seen in

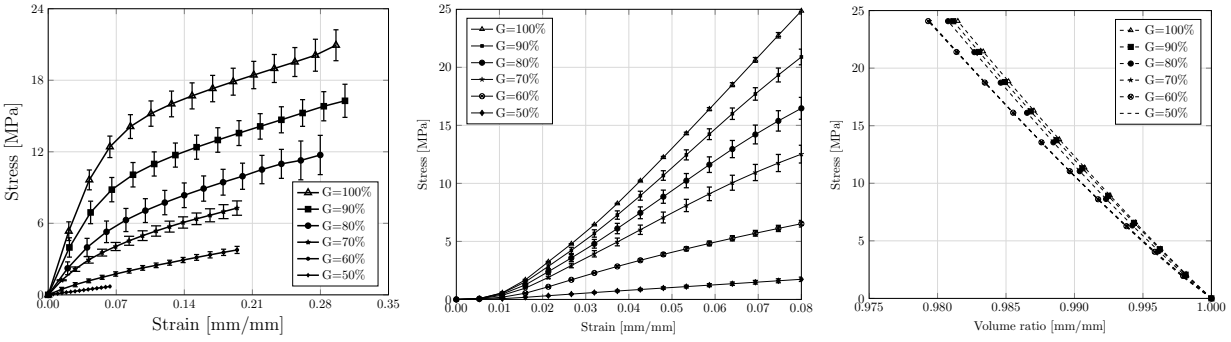

(a) Uniaxial tension **(b)** Uniaxial compression **(c)** Volumetric compression

Figure 3: Results of experimental tests for material characterization at grayscales $G = 100\%$ to $G = 50\%$. In (a) and (b), the ranges of experimental results are indicated by the shaded areas, while in (c) the averages are shown, since experiments exhibit little variation.

G	d [1/MPa]	C_{10}	C_{01}	C_{11}	κ	μ	E	ν [·]
100%	$1.57 \cdot 10^{-3}$	-141.1	182.5	41.02	1274	82.68	242.8	0.4682
90%	$1.67 \cdot 10^{-3}$	-130.2	162.8	44.72	1194	65.14	191.9	0.4732
80%	$1.74 \cdot 10^{-3}$	-113.8	137.9	45.43	1151	48.60	143.8	0.4791
70%	$1.83 \cdot 10^{-3}$	-65.29	81.08	26.49	1091	31.41	93.34	0.4857
60%	$1.85 \cdot 10^{-3}$	-50.71	58.25	26.22	1082	17.19	51.30	0.4921
50%	$1.91 \cdot 10^{-3}$	-7.587	10.07	0.014	1048	4.936	14.79	0.4976

Table 2: Mooney-Rivlin coefficients and physical material parameters (all in MPa, except d and ν) obtained by curve fitting of the experimental results for each grayscale.

Fig. 6, too.

Generally, the increase of stiffness with increasing G can be explained with the increase of cross-linking density. This also contributes to the higher failure strains and stresses that can be observed in uniaxial tension tests in Fig. 3a. Furthermore, lower cross-linking density means that the material remains in a more liquid state, which explains that the Poisson's ratio approaches 0.5 with decreasing G. As mentioned, for $G < 50\%$ the cross-linking density is very low and the material remains liquid.

3.2. Interpolation and validation of parametric material model

The material models and their coefficients and parameters obtained in the previous Subsection can be implemented into a finite element method to predict and investigate the behavior of objects printed at the different grayscale values under arbitrary loading conditions. However, the major advantage of the grayscale printing technique is that it allows for tailoring of material properties throughout a structure by arbitrary variation and grading of grayscale values. Thus, the Mooney-Rivlin coefficients obtained for different grayscale values are now parameterized using linear and quadratic approximations, see Fig. 5. Calculating the Lamé parameters from the interpolated material constants shows the same monotonous behavior, see Fig. 6. Although various interpolations or approximations are possible, the behavior of the Lamé parameters is not very sensitive to these changes and the combinations of coefficients lead to very similar overall constitutive responses of the material. Thus, we proceed by using the quadratic parameterization in terms of G throughout the remainder of the manuscript.

Now, we want to verify that the interpolated Mooney-Rivlin coefficients yield reasonable material models for any $50\% \leq G \leq 100\%$, i.e., that our parametric hyperelastic constitutive model can be applied to arbitrary grayscale values as they may appear in functionally graded objects. Thus, we compare the stress-strain curves for uniaxial ten-

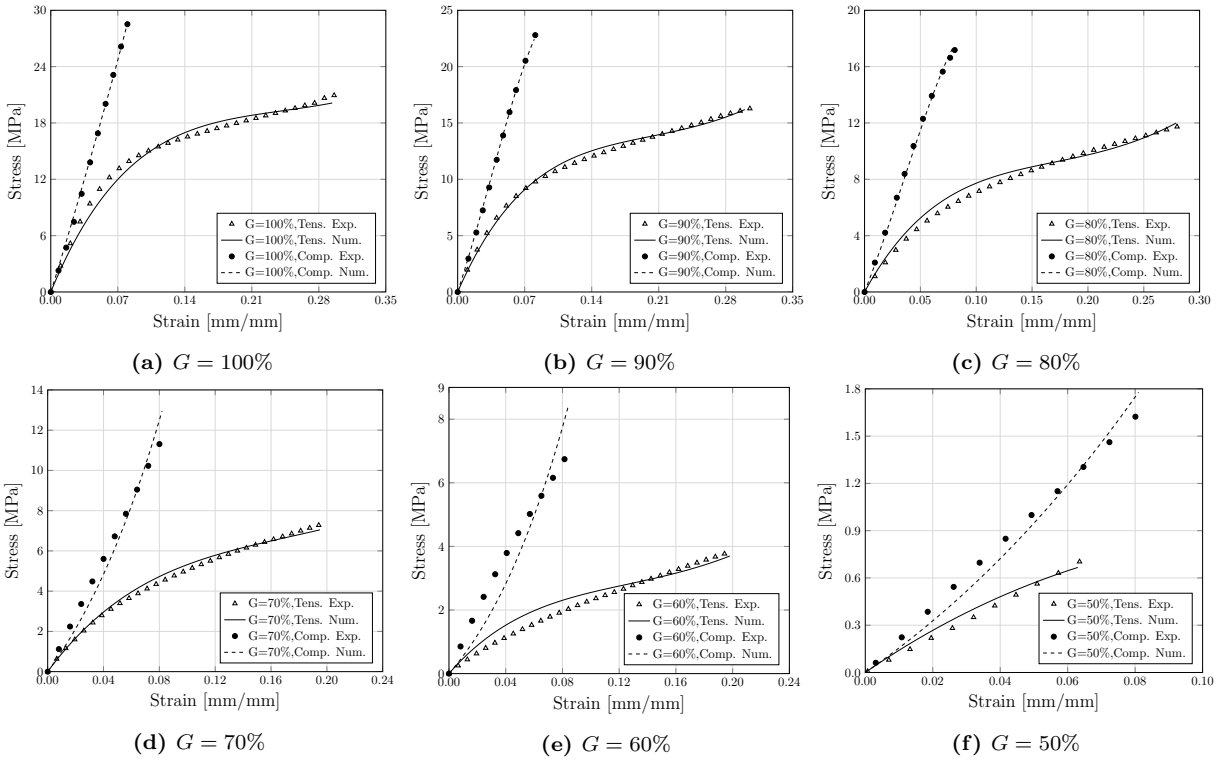

(a) $G = 100\%$ **(b)** $G = 90\%$ **(c)** $G = 80\%$

(d) $G = 70\%$ **(e)** $G = 60\%$ **(f)** $G = 50\%$

Figure 4: Comparison of averaged experimental stress-strain curves with fitted hyperelastic material model for uniaxial tension and uniaxial compression tests for grayscales $G = 100\%$ to $G = 50\%$.

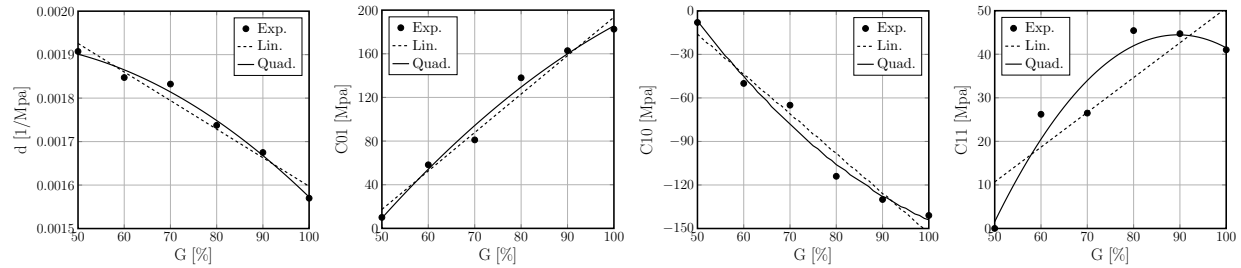

Figure 5: Mooney-Rivlin coefficients $d, C_{01}, C_{10}, C_{11}$ obtained by curve fitting of the experimental results for each grayscale. Linear and quadratic approximations parameterize the grayscales between experimental data.

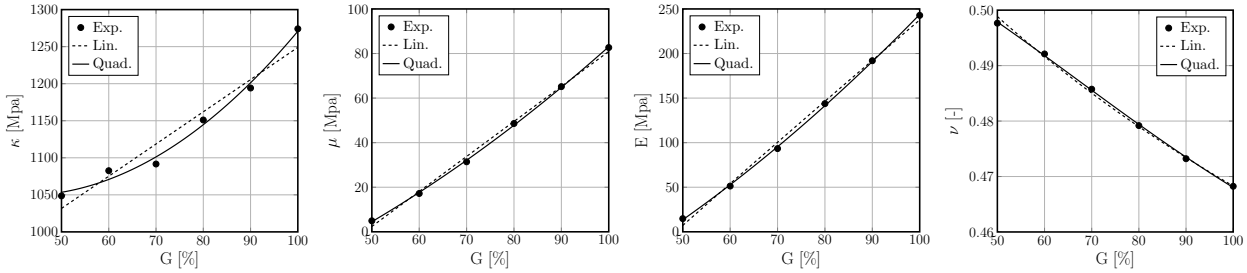

Figure 6: Physical material parameters bulk modulus κ, shear modulus μ, Young's modulus E, and Poisson's ratio ν obtained by curve fitting of the experimental results for each grayscale. Linear and quadratic approximations parameterize the grayscales between experimental data.

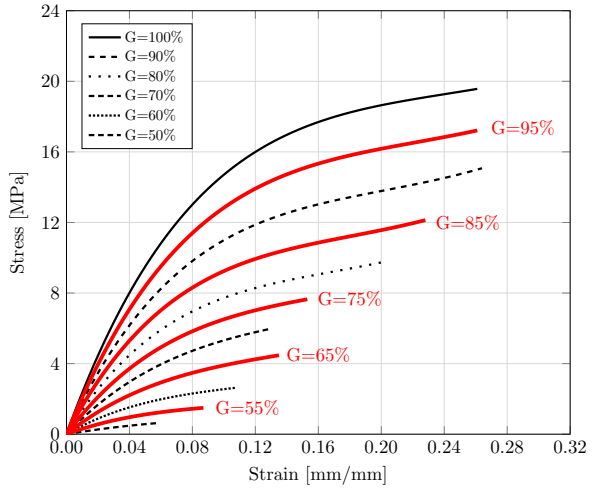

Figure 7: Comparison of the uniaxial tension stress-strain curves obtained from the experimentally fitted material models with the interpolated models for $G = 95\%, G = 85\%, G = 75\%$, and $G = 65\%$.

sion obtained for the experimentally fitted and validated grayscale values of $G = 100\%, G = 90\%, G = 80\%, G = 70\%, G = 60\%$, and $G = 50\%$, which were used to calibrate the material models, with the "arbitrary" values $G = 95\%, G = 85\%, G = 75\%$, and $G = 65\%$, for which the curves are obtained by interpolating the coefficients for given G as in Fig. 5 and then numerically evaluating the Mooney-Rivlin model using equation (7). Figure 7 shows that the stress-strain curves for the interpolated grayscales assume reasonable values and each lay between the ones for the calibrated models, e.g., $G = 95\%$ is in between $G = 100\%$ and $G = 90\%$.

3.3. Applications and validations for graded structures

To further validate the parametric hyperelastic constitutive model for grayscale MSLA-printed materials for practical applications, three examples with continuously graded grayscale designs are investigated. To avoid a strong influence of geometrical nonlinearities and instabilities in validation of the material behavior and to capture the material model to the failure point, the tests are carried out in tension.

Graded rectangle. Figure 8 presents a rectangular plate of width 50 mm, height 120 mm and thickness 2 mm, in which the grayscale value varies linearly from $G = 60\%$ to $G = 100\%$ from left to right, see Fig. 8a, and thus also the material properties, see Fig. 8b and c. The sample is clamped in a tensile testing machine and stretch in the direction orthogonal to the material variation. Figure 8d shows the sample simulated with grayscale material model at an applied strain of 9.5%, colored by the stress component P_{11}, Fig. 8e a photo of the printed sample in the experiment right before failure at 9.5% strain and Fig. 8f after material failure at 10% strain. Comparing the failed sample and the simulation reveals that stress concentrations occur in the right corners, where the grayscale is $G = 100\%$, i.e., the sample is the stiffest, but the failure stress is already reached, since it is in between uniaxial tension and compression states, compare Fig. 4a. Further, comparing numerical and experimental stress-strain curves in Fig. 8g shows a good agreement. The numerical stress is obtained by averaging the stress at the boundary of the geometry and the experimental stress is the reaction force measured by the tensile test machine divided by the cross-section area of the sample. The strain is obtained from the displacement prescribed by the tensile testing machine divided by the height of the sample. The same evaluation is carried out for the subsequent test cases. There are some deviations for higher values of strain, where the maximum and average absolute errors increase to almost 0.78 MPa and 0.47 MPa, respectively, which yield the maximum relative error of 6.5%, which is still a good approximation.

Graded plate with hole. The next validation is carried out with the classical example of a rectangular plate with a hole, which is also investigated under tensile loading, see Fig. 9. The geometric parameters are the same as in the previous example, just that a hole of diameter 22.5 mm is added in the center of the plate. The grading is again linear in orthogonal direction to tension from $G = 100\%$ to $G = 60\%$, as shown in Fig. 9a. Consequently, the material properties of the printed sample alter from left to right as demonstrated in Fig. 9b and c. Figure 9d shows the sample simulated with grayscale material model at an applied strain of 5.3%, colored by the stress component P_{11}, Fig. 9e a photo of the printed sample in the experiment before failure at 5.3% strain and Fig. 9f at material failure at 5.6% strain. Here, a good agreement of the simulated deformation and the deformed sample in the experiment can be observed visually. Further, the stress distribution in the simulated sample shows

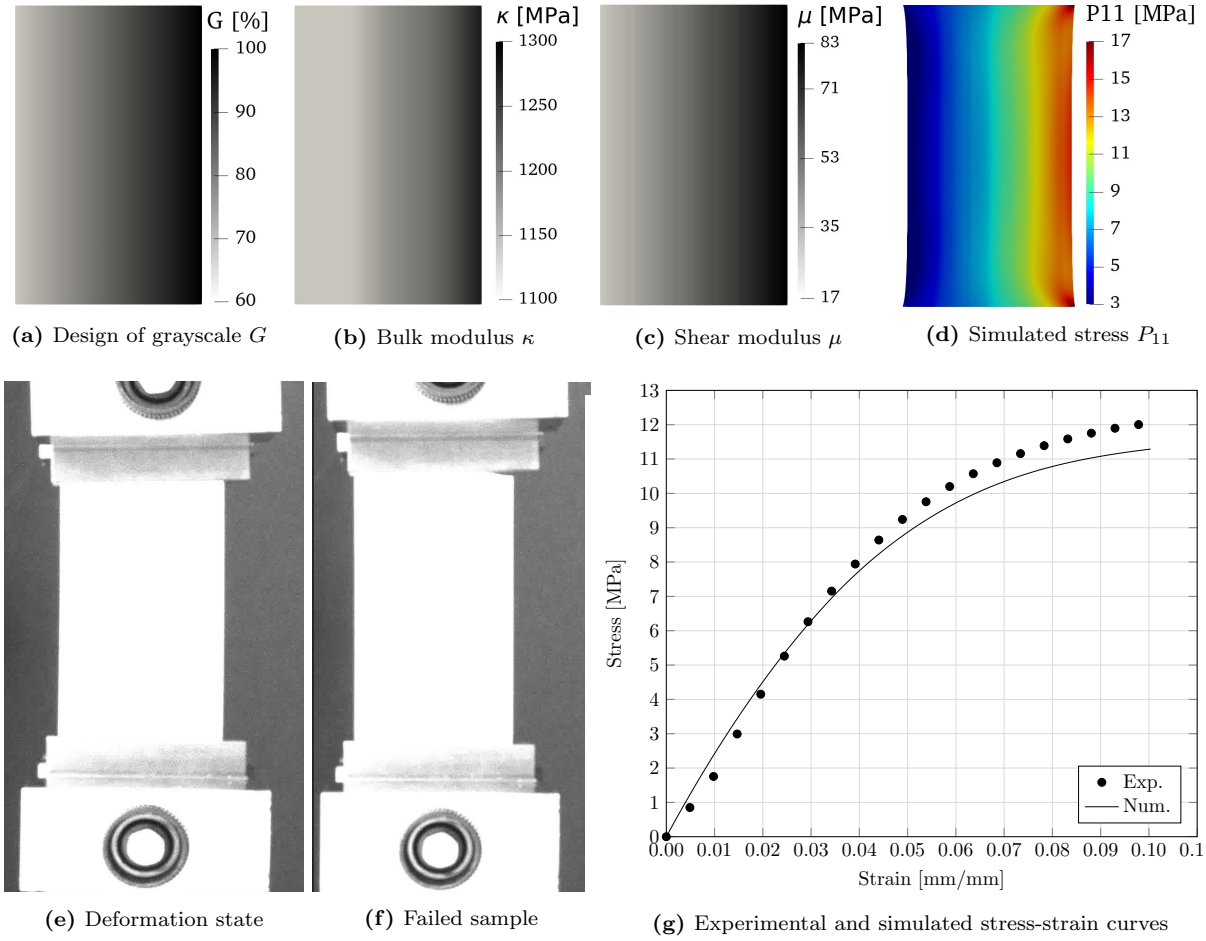

(a) Design of grayscale G **(b)** Bulk modulus κ **(c)** Shear modulus μ **(d)** Simulated stress P_{11}

(e) Deformation state **(f)** Failed sample **(g)** Experimental and simulated stress-strain curves

Figure 8: A graded rectangle in which the grayscale varies linearly from $G = 60\%$ to $G = 100\%$ and the material properties change orthogonal to the tension direction, see (a) to (c). (d) shows the simulated stress distribution and the deformation state. The deformed shapes right before and after failure in the experiment are shown in (e) and (f), respectively. The experimental and numerical stress-strain curves are compared in (g).

the stress concentration on the failed area in experiments, where $G \approx 90\%$ and $P_{11} \approx 15$ MPa. Additionally, the stress-strain curves for numerical and experimental calculations are illustrated and compared in Fig. 9g, which shows a good agreement between both numerical and experimental results. Again, there are some deviations for higher strain values, which leads to the maximum and average absolute errors of about 0.8 MPa and 0.24 MPa, respectively, and a maximum relative error of about 12%.

Graded trapezoid. The final validation case is a graded trapezoid, see Fig. 10. The height of the trapezoid is 120 mm, the bottom width 60 mm, the top width 20 mm, and the thickness 2 mm. Now, the grayscale varies linearly from bottom to top from $G = 60\%$ to $G = 100\%$, see Fig. 10a, and thus the material properties change along tensile direction, see Fig. 10b and c. The simulated deformation shown in Fig. 10d at 5.3% strain shows reasonable agreement with the deformed state in the experiment shown in Fig. 10e. Interestingly, the failure shown in Fig. 10f occurs not at the point of maximum stress, but somewhere towards the bottom, where the softer material fails more easily. Comparing the numerical and experimental stress-strain curves in Fig. 10g shows very good agreement between the numerical model and experimental results. The maximum and average absolute errors are about 0.24 MPa and 0.17 MPa respectively, which lead to a maximum relative error of 2.5%,

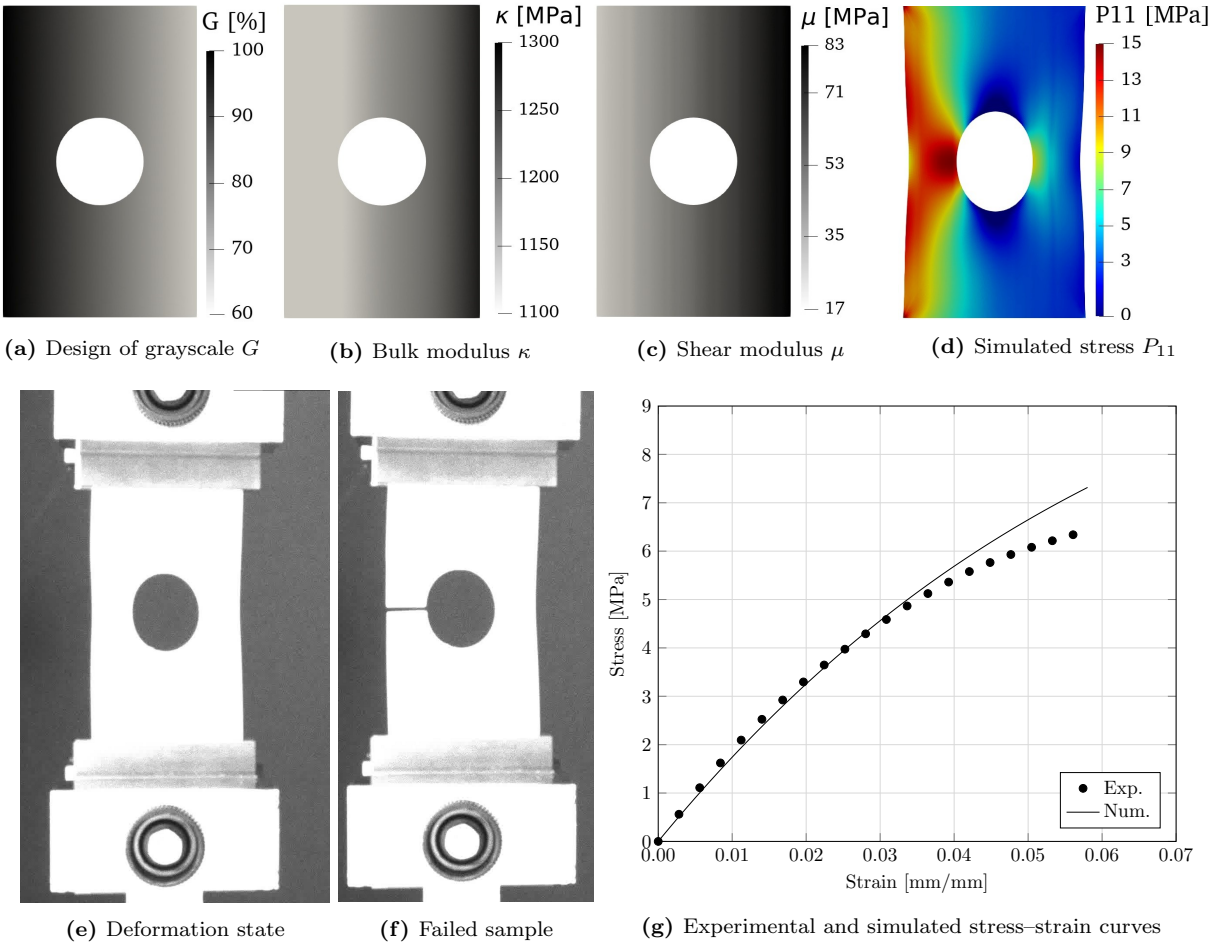

(a) Design of grayscale G **(b)** Bulk modulus κ **(c)** Shear modulus μ **(d)** Simulated stress P_{11}

(e) Deformation state **(f)** Failed sample **(g)** Experimental and simulated stress–strain curves

Figure 9: A graded rectangle with hole in which the grayscale varies linearly from $G = 100\%$ to $G = 60\%$ and the material properties change orthogonal to the tension direction, see (a) to (c). (d) shows the simulated stress distribution and the deformation state. The deformed shapes right before and after failure in the experiment are shown in (e) and (f), respectively. The experimental and numerical stress-strain curves are compared in (g).

which is a good approximation of experimental results.

4. Conclusion

We have presented the application of grayscale masked stereolithography (MSLA) for the design and manufacturing of functionally graded parts with spatially varying material properties, that can be subject to finite deformations. For this purpose, a hyperelastic constitutive model was developed that includes the parametric dependency on the grayscale value, which essentially controls light intensity and thus the degree of curing of UV-curable photopolymer materials. In particular, the Mooney-Rivlin hyperelastic constitutive model with three coefficients has been utilized. Performing uniaxial tension and compression, and volumetric tension tests on specimens printed at different grayscales of $G = 100\%, G = 90\%, G = 80\%, G = 70\%, G = 60\%$, and $G = 50\%$, these material coefficients were first experimentally fitted and then interpolated to obtain a parametric material model in terms of the grayscale G. The Mooney-Rivlin coefficients showed (almost) monotonous behavior in terms of the grayscale and they lead to an almost linear dependency of the physical material properties, namely Young's modulus, bulk modulus, shear modulus, and Poisson's ratio, on G. Thus, these linearly or quadratically approximated coefficients lead to valid and reasonable physical properties and stress-strain curves. Finally, the resulting mate-

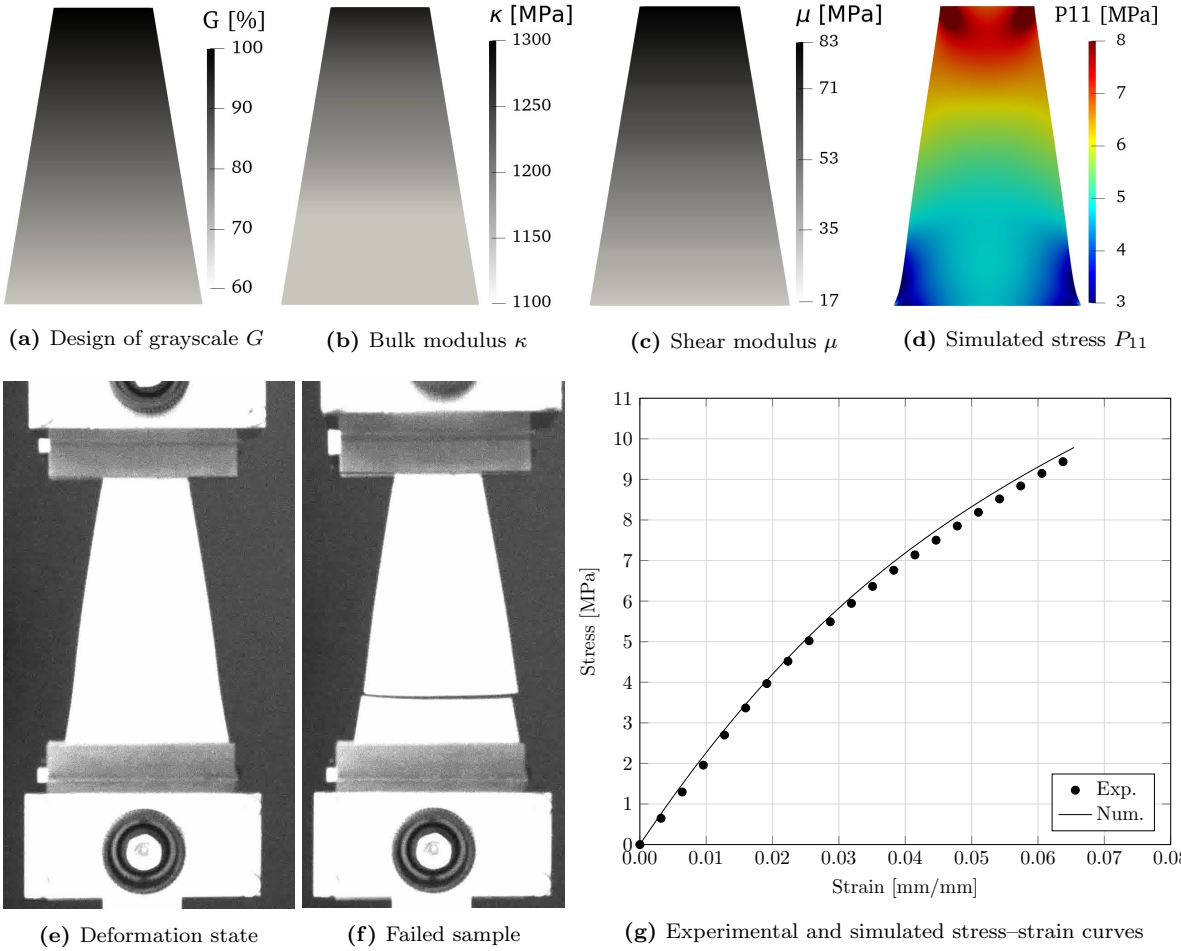

(a) Design of grayscale G **(b)** Bulk modulus κ **(c)** Shear modulus μ **(d)** Simulated stress P_{11}

(e) Deformation state **(f)** Failed sample **(g)** Experimental and simulated stress–strain curves

Figure 10: A graded trapezoid in which the grayscale varies linearly from $G = 100\%$ to $G = 60\%$ and the material properties change in the tension direction, see (a) to (c). (d) shows the simulated stress distribution and the deformation state. The deformed shapes right before and after failure in the experiment are shown in (e) and (f), respectively. The experimental and numerical stress-strain curves are compared in (g).

rial model was implemented into a finite element method and validated experimentally using three test cases for different plate-like geometries with continuous, linear grading of grayscale.

The investigations and observations have revealed that the MSLA 3D printing technique can realize graded parts with hyperelastic material properties. This opens new perspectives for the design of graded polymer structures with tuneable mechanical behavior even at finite deformations. Here, the characterization of the parametric hyperelastic material model was carried out for a commercially available, UV-curable resin. However, in the future similar investigations should also be carried out for other types of photosensitive polymers or hydrogels with improved properties, such as higher stiffness, higher failure strains or stresses, as well as functional behaviors such as shape-memory effect, stimuli-responsiveness, etc. Furthermore, transient and cyclic behavior can be crucial for practical applications, which suggests the extension of the material model towards visco-elasticity, as well as inelastic effects such as Mullins effect or plasticity.

Acknowledgements

We are thankful to our colleagues Tannaz Tayyarian at the Catholic University of America, Washington, D.C., who provided expertise in the theory of polymerization that greatly assisted the research, and Armin Asheri at TU Darmstadt for assistance with simulations of test cases.

References

[1] A.P. Zhang, X. Qu, P. Soman, K.C. Hribar, J.W. Lee, S. Chen, S. He, Rapid fabrication of complex 3D extracellular microenvironments by dynamic optical projection stereolithography, Adv. Mater. 24 (2012) 4266–4270. https://doi.org/10.1002/adma.201202024.

[2] J. Warner, P. Soman, W. Zhu, M. Tom, S. Chen, Design and 3D printing of hydrogel Scaffolds with fractal geometries, ACS Biomater. Sci. Eng. 2 (2016) 1763–1770. https://doi.org/10.1021/acsbiomaterials.6b00140.

[3] B. Esmaeilian, S. Behdad, B. Wang, The evolution and future of manufacturing: A review, J. Manuf. Syst. 39 (2016) 79–100. https://doi.org/10.1016/j.jmsy.2016.03.001.

[4] S.H. Pyo, P. Wang, H.H. Hwang, W. Zhu, J. Warner, S. Chen, Continuous optical 3D printing of green aliphatic polyurethanes, ACS Appl. Mater. Interfaces 9 (2017) 836–844. https://doi.org/10.1021/acsami.6b12500.

[5] Q. Ge, Z. Li, Z. Wang, K. Kowsari, W. Zhang, X. He, J. Zhou, N.X. Fang, Projection micro stereolithography based 3D printing and its applications, Int. J. Extrem. Manuf. 2 (2020), 022004. https://doi.org/10.1088/2631-7990/ab8d9a.

[6] E.J.P. Jansen, R.E.J. Sladek, H. Bahar, A. Yaffe, M.J. Gijbels, R. Kuijer, S.K. Bulstra, N.A. Guldemond, I. Binderman, L.H. Koole, Hydrophobicity as a design criterion for polymer scaffolds in bone tissue engineering, Biomaterials 26 (2005) 4423–4431. https://doi.org/10.1016/j.biomaterials.2004.11.011.

[7] S.V. Murphy, A. Atala, 3D bioprinting of tissues and organs, Nat. Biotechnol. 32 (2014) 773–785. https://doi.org/10.1038/nbt.2958.

[8] C.L. Ventola, Medical applications for 3D printing-current and projected uses, Pharm. Ther. 39 (2014) 704–711.

[9] K. Markstedt, A. Mantas, I. Tournier, H. Martínez Ávila, D. Hägg, P. Gatenholm, 3D bioprinting human chondrocytes with nanocellulose-alginate bioink for cartilage tissue engineering applications, Biomacromolecules 16 (2015) 1489–1496. https://doi.org/10.1021/acs.biomac.5b00188.

[10] K. Qiu, Z. Zhao, G. Haghiashtiani, S.Z. Guo, M. He, R. Su, Z. Zhu, D.B. Bhuiyan, P. Murugan, F. Meng, S.H. Park, C.C. Chu, B.M. Ogle, D.A. Saltzman, B.R. Konety, R.M. Sweet, M.C. McAlpine 3D Printed organ models with physical properties of tissue and integrated sensors, Advanced Materials Technologies 3 (2018) 1700235. https://doi.org/10.1002/admt.201700235.

[11] F. Yang, M. Zhang, B. Bhandari, Recent development in 3D food printing, Crit. Rev. Food Sci. Nutr. 57 (2017) 3145–3153. https://doi.org/10.1080/10408398.2015.1094732.

[12] X. Zheng, H. Lee, T.H. Weisgraber, M. Shusteff, J. DeOtte, E.B. Duoss, J.D. Kuntz, M.M. Biener, Q. Ge, J.A. Jackson, S.O. Kucheyev, N.X. Fang, C.M. Spadaccini, Ultralight, ultrastiff mechanical metamaterials, Science 344 (2014) 1373–1377. https://doi.org/10.1126/science.1252291.

[13] J.A. Jackson, M.C. Messner, N.A. Dudukovic, W.L. Smith, L. Bekker, B. Moran, A.M. Golobic, A.J. Pascall, E.B. Duoss, K.J. Loh, C.M. Spadaccini, Field responsive mechanical metamaterials, Sci. Adv. 4, eaau6419. https://doi.org/10.1126/sciadv.aau6419.

[14] Y. Kim, H. Yuk, R. Zhao, S.A. Chester, X. Zhao, Printing ferromagnetic domains for untethered fast-transforming soft materials, Nature 558 (2018) 274–279. https://doi.org/10.1038/s41586-018-0185-0.

[15] X. Kuang, K. Chen, C.K. Dunn, J. Wu, V.C.F. Li, H.J. Qi, 3D printing of highly stretchable, shape-memory and self-healing elastomer toward novel 4D printing, ACS Appl. Mater. Interfaces 10 (2018) 7381–7388. https://doi.org/10.1021/acsami.7b18265.

[16] Z. Ding, C. Yuan, X. Peng, T. Wang, H.J. Qi, M.L. Dunn, Direct 4D printing via active composite materials, Sci. Adv. 3 (2017), e1602890. https://doi.org/10.1126/sciadv.1602890.

[17] Z. Zhao, J. Wu, X. Mu, H. Chen, H.J. Qi, D. Fang, Origami by frontal photopolymerization, Sci. Adv. 3 (2017), e1602326. https://doi.org/10.1126/sciadv.1602326.

[18] X. Kuang, D.J. Roach, J. Wu, C.M. Hamel, Z. Ding, T. Wang, M.L. Dunn, H.J. Qi, Advances in 4D Printing: Materials and Applications, Adv. Funct. Mater., Part B: Polym. Phys. 29 (2019), 1805290. https://doi.org/10.1002/adfm.201805290.

[19] X. Kuang, J. Wu, K. Chen, Z. Zhao, Z. Ding, F. Hu, D. Fang, H.J. Qi, Grayscale digital light processing 3D printing for highly functionally graded materials, Sci. Adv. 5 (2019), eaav5790. https://doi.org/10.1126/sciadv.aav5790.

[20] Q. Zhang, X. Kuang, S. Weng, Z. Zhao, H. Chen, D. Fang, H.J. Qi, Rapid volatilization induced mechanically robust shape-morphing structures toward 4D printing, ACS Appl. Mater. Interfaces 12 (2020) 17979–17987. https://doi.org/10.1021/acsami.0c02038.

[21] T.S. Wei, B.Y. Ahn, J. Grotto, J.A. Lewis, 3D printing of customized Li-ion batteries with thick electrodes, Adv. Mater. 30 (2018), 1703027. https://doi.org/10.1002/adma.201703027.

[22] D. Espalin, D.W. Muse, E. MacDonald, R.B. Wicker, 3D Printing multifunctionality: Structures with electronics, Int. J. Adv. Manuf. Technol. 72 (2014) 963–978. https://doi.org/10.1007/s00170-014-5717-7.

[23] J.A. Lewis, B.Y. Ahn, Device fabrication: Three-dimensional printed electronics, Nature 518 (2015) 42–43. https://doi.org/10.1038/518042a.

[24] I. Gibson, D. Rosen, B. Stucker, Additive Manufacturing Technologies: 3D Printing, Rapid Prototyping, and Direct Digital Manufacturing, Springer, New York, 2015.

[25] M. Layani, X. Wang, S. Magdassi, Novel Materials for 3D Printing by Photopolymerization, Adv. Mater. 30 (2018) 1706344. https://doi.org/10.1002/adma.201706344.

[26] M. Pagac, J. Hajnys, Q.P. Ma, L. Jancar, J. Jansa, P. Stefek, J. Mesicek, A review of vat photopolymerization technology: Materials, applications, challenges, and future trends of 3d printing, Polymers 13 (2021) 1–20. https://doi.org/10.3390/polym13040598.

[27] A. Garland, G. Fadel, Design and Manufacturing Functionally Gradient Material Objects with an off the Shelf Three-Dimensional Printer: Challenges and Solutions, J. Mech. Des. Trans. ASME. 137 (2015). https://doi.org/10.1115/1.4031097.

[28] B. Zhang, P. Jaiswal, R. Rai, S. Nelaturi, Additive manufacturing of functionally graded objects: A review, Proc. ASME Des. Eng. Tech. Conf., American Society of Mechanical Engineers (ASME), 2016. https://doi.org/10.1115/DETC2016-60320.

[29] G.H. Loh, E. Pei, D. Harrison, M.D. Monzón, An overview of functionally graded additive manufacturing, Addit. Manuf. 23 (2018) 34–44. https://doi.org/10.1016/j.addma.2018.06.023.
[30] A. Bandyopadhyay, B. Heer, Additive manufacturing of multi-material structures, Mater. Sci. Eng. R Reports. 129 (2018) 1–16. https://doi.org/10.1016/j.mser.2018.04.001.
[31] N. Oxman, Variable property rapid prototyping, Virtual Phys. Prototyp. 6 (2011) 3–31. https://doi:10.1080/17452759.2011.558588.
[32] O. Weeger, Y.S.B. Kang, S.K. Yeung, M.L. Dunn, Optimal Design and Manufacture of Active Rod Structures with Spatially Variable Materials, 3D Print. Addit. Manuf. 3 (2016) 205–215. https://doi.org/10.1089/3dp.2016.0039.
[33] I.F. Ituarte, N. Boddeti, V. Hassani, M.L. Dunn, D.W. Rosen, Design and additive manufacture of functionally graded structures based on digital materials, Addit. Manuf. 30 (2019) 100839. https://doi.org/10.1016/j.addma.2019.100839.
[34] Q. Ge, A.H. Sakhaei, H. Lee, C.K. Dunn, N.X. Fang, M.L. Dunn, Multimaterial 4D printing with tailorable shape memory polymers, Sci. Rep. 6 (2016) 1-11. https://doi.org/10.1038/srep31110.
[35] K. Kowsari, S. Akbari, D. Wang, N.X. Fang, Q. Ge, High-efficiency high-resolution multimaterial fabrication for digital light processing-based three-dimensional printing, 3D Print. Addit. Manuf. 5 (2018) 185–193. https://doi.org/10.1089/3dp.2018.0004.
[36] Y. Lu, G. Mapili, G. Suhali, S. Chen, K. Roy, A digital micro-mirror device-based system for the microfabrication of complex, spatially patterned tissue engineering scaffolds, J. Biomed. Mater. Res. 77 (2006) 396–405. https://doi.org/10.1002/jbm.a.30601.
[37] J.H. Na, N.P. Bende, J. Bae, C.D. Santangelo, R.C. Hayward, Grayscale gel lithography for programmed buckling of non-Euclidean hydrogel plates, Soft Matter 12 (2016) 4985–4990. https://doi.org/10.1039/c6sm00714g.
[38] D. Xue, Y. Wang, D. Mei, Multi-step exposure method for improving structure flatness in digital light processing-based printing, J. Manuf. Process. 39 (2019) 106–113. https://doi.org/10.1016/j.jmapro.2019.02.013.
[39] D.B. Kolesky, R.L. Truby, A.S. Gladman, T.A. Busbee, K.A. Homan, J.A. Lewis, 3D Bioprinting of Vascularized, Heterogeneous Cell-Laden Tissue Constructs mask, Advanced Materials 26 (2014) 3124–3130. https://doi.org/10.1002/adma.201305506.
[40] Q. Mu, L. Wang, C.K. Dunn, X. Kuang, F. Duan, Z. Zhang, H.J. Qi, T. Wang, Digital light processing 3D printing of conductive complex structures, Addit. Manuf. 18 (2017) 74–83. https://doi.org/10.1016/j.addma.2017.08.011.
[41] S.C.P. Norris, P. Tseng, A.M. Kasko, Direct Gradient Photolithography of Photodegradable Hydrogels with Patterned Stiffness Control with Submicrometer Resolution, ACS Biomater. Sci. Eng. 2 (2016) 1309–1318. https://doi.org/10.1021/acsbiomaterials.6b00237.
[42] G.I. Peterson, J.J. Schwartz, D. Zhang, B.M. Weiss, M.A. Ganter, D.W. Storti, A.J. Boydston, Production of Materials with Spatially-Controlled Cross-Link Density via Vat Photopolymerization, ACS Appl. Mater. Interfaces 8 (2016) 29037–29043. https://doi.org/10.1021/acsami.6b09768. J. Mech. Phys. Solids 112 (2018) 25–49. https://doi.org/10.1016/j.jmps.2017.11.018
[43] J. Wu, Z. Zhao, C.M. Hamel, X. Mu, X. Kuang, Z. Guo, H.J. Qi, Evolution of material properties during free radical photopolymerization, J. Mech. Phys. Solids 112 (2018) 25–49. https://doi.org/10.1016/j.jmps.2017.11.018.
[44] J. Wu, Z. Zhao, X. Kuang, C.M. Hamel, D. Fang, H.J. Qi, Reversible shape change structures by grayscale pattern 4D printing, Multifunctional Mater. 1 (2018), 015002. https://doi.org/10.1088/2399-7532/aac322.
[45] Z. Zhao, J. Wu, X. Mu, H. Chen, H.J. Qi, D. Fang, Desolvation Induced Origami of Photocurable Polymers by Digit Light Processing, Macromol. Rapid Commun. 38 (2016), 1600625. https://doi.org/10.1002/marc.201600625.
[46] Y. Xiang, C. Schilling, N. Arora, A.J. Boydston, S. Rudykh, Mechanical characterization and constitutive modeling of visco-hyperelasticity of photocured polymers, Addit. Manuf. 36 (2020), 101511. https://doi.org/10.1016/j.addma.2020.101511.
[47] M. Robinson, S. Soe, R. Johnston, R. Adams, B. Hanna, R. Burek, G. McShane, R. Celeghini, M. Alves, P. Theobald, Mechanical characterisation of additively manufactured elastomeric structures for variable strain rate applications, Addit. Manuf. 27 (2019) 398–407. https://doi.org/10.1016/j.addma.2019.03.022.
[48] J. Liljenhjerte, P. Upadhyaya, S. Kumar, Hyperelastic strain measurements and constitutive parameters identification of 3D printed soft polymers by image processing, Addit. Manuf. 11 (2016) 40–48. https://doi.org/10.1016/j.addma.2016.03.005.
[49] F.F. Abayazid, M. Ghajari, Material characterisation of additively manufactured elastomers at different strain rates and build orientations, Addit. Manuf. 33 (2020), 101160. https://doi.org/10.1016/j.addma.2020.101160.
[50] Z. Zhao, D. Wu, H. Chen, H.J. Qi, D. Fang, Indentation experiments and simulations of nonuniformly photocrosslinked polymers in 3D printed structures, Addit. Manuf. 35 (2020) 101420. https://doi.org/10.1016/j.addma.2020.101420.
[51] S. Hartmann, Numerical studies on the identification of the material parameters of Rivlin's hyperelasticity using tension-torsion tests, Acta Mech. 148 (2001) 129–155. https://doi.org/10.1007/BF01183674.
[52] R.S. Rivlin, D.W. Saunders, Large elastic deformations of isotropic materials VII. Experiments on the deformation of rubber, Philos. Trans. R. Soc. A 243 (1951) 251–288. https://doi.org/10.1098/rsta.1951.0004.
[53] T.Y.P. Chang, A.F. Saleeb, G. Li, Large strain analysis of rubber-like materials based on a perturbed Lagrangian variational principle, Comput. Mech. 8 (1991) 221–233. https://doi.org/10.1007/BF00577376.
[54] K. Upadhyay, G. Subhash, D. Spearot, Hyperelastic constitutive modeling of hydrogels based on primary deformation modes and validation under 3D stress states, International Journal of Engineering Science 154 (2020) 103314. https://doi.org/10.1016/j.ijengsci.2020.103314.
[55] M. Bodaghi, A.R. Damanpack, G.F. Hu, W.H. Liao, Large deformations of soft metamaterials fabricated by 3D printing, Mater. Des. 131 (2017) 81–91. https://doi.org/10.1016/j.matdes.2017.06.002.
[56] M. Bodaghi, W.H. Liao, 4D printed tunable mechanical metamaterials with shape memory oper-

ations, Smart Mater. Struct. 28 (2019) 045019. https://doi.org/10.1088/1361-665X/ab0b6b.
[57] Prusa Research a.s., https://www.prusa3d.com, 2021.
[58] Y. Wang, D. Xue, D. Mei, Projection-Based Continuous 3D Printing Process With the Grayscale Display Method, J. Manuf. Sci. Eng. 142 (2020) 021003. https://doi.org/10.1115/1.4045616.
[59] A. Bertsch, J.Y. Jézéquel, J.C. André, Study of the spatial resolution of a new 3D microfabrication process: The microstereophotolithography using a dynamic mask-generator technique, J. Photochem. Photobiol. A: Chem 107 (1997) 275–281. https://doi.org/10.1016/S1010-6030(96)04585-6.
[60] A. Vitale, M.G. Hennessy, O.K. Matar, J.T. Cabral, Interfacial profile and propagation of frontal photopolymerization waves, Macromolecules 48 (2015) 198–205. https://doi.org/10.1021/ma5021215.
[61] J.C. Dizon, A.H. Espera Jr., Q. Chen, R.C. Advincula, Mechanical characterization of 3D-printed polymers, Addit. Manuf. 20 (2018) 44–67. https://doi.org/10.1016/j.addma.2017.12.002
[62] S. Wang, Y. Ma, Z. Deng, K. Zhang, S. Dai, Implementation of an elastoplastic constitutive model for 3D-printed materials fabricated by stereolithography, Addit. Manuf. 33 (2020) 101104. https://doi.org/10.1016/j.addma.2020.101104
[63] C. Decker, Photoinitiated crosslinking polymerisation, Prog. Polym. Sci. 21 (1996) 593–650. https://doi.org/10.1016/0079-6700(95)00027-5.
[64] C. Hofstetter, S. Orman, S. Baudis, J. Stampfl, Combining cure depth and cure degree, a new way to fully characterize novel photopolymers, Addit. Manuf. 24 (2018) 166–172. https://doi.org/10.1016/j.addma.2018.09.025.
[65] G.A. Holzapfel, Nonlinear Solid Mechanics: A Continuum Approach for Engineering, Wiley, Chichester, England, 2000.
[66] R.S. Rivlin, Large elastic deformations of isotropic materials IV. further developments of the general theory, Philos. Trans. R. Soc. A 241 (1948) 379–397. https://doi.org/10.1098/rsta.1948.0024.
[67] R.W. Ogden, G. Saccomandi, I. Sgura, Fitting hyperelastic models to experimental data, Comput. Mech. 34 (2004) 484–502. https://doi.org/10.1007/s00466-004-0593-y.
[68] MATLAB, version 9.8.0.1451342 (R2020a), The MathWorks Inc. Natick, Massachusetts.